A Blade Element Approach to Modeling Aerodynamic Flight of an Insect-scale Robot

Taylor S. Clawson[1] *Student Member, IEEE,* Sawyer B. Fuller[2],
Robert J. Wood[3] *Senior Member, IEEE*, and Silvia Ferrari[1] *Senior Member, IEEE*

***Abstract*— Recent manufacturing advances have allowed for the creation of gram and sub-gram *insect*-scale flapping robots. Most dynamic models of such robots to date have either assumed stroke-averaged forces or did not account for body motion. In order to design more robust and capable control methods, this paper incorporates blade element theory with a rigid-body dynamic model to calculate instantaneous aerodynamic forces during each wing stroke. As a result, the model accurately predicts body motions during flight.**

I. Introduction

Recent advances in manufacturing technologies have paved the way for the creation of gram and sub-gram *insect*-scale flapping robots [1]. Due to their small size and light weight, these robots are potentially capable of exploring small spaces and maneuvering in confined spaces or narrow passages. These robots also benefit from increased survivability through force-scaling effects [2].

Many approaches to designing Micro-Aerial Vehicles (MAVs) begin to break down at the centimeter-scale. For instance, the motors used in quadrotor designs become less efficient at smaller sizes as friction forces begin to dominate the desired torque generated by the motor [1]. Flapping wing designs using piezoelectric actuators do not suffer from the same scaling issues, and thus have wide ranging future applications. Their size allows them to maneuver through tight spaces, as in search and rescue applications, where rubble or other obstructions can make it difficult to reach a target. Also, a swarm of smaller robots can be deployed as cheaply as a single larger robot and have a greater likelihood of detecting a target while surviving a hazardous environment. Other potential uses include sensing and surveillance, where their small size can make them inherently difficult to track.

The RoboBee, shown in Fig. 1, is an insect-scale robot that can hover, follow commanded trajectories, perch, and even travel underwater [3], [4]. It is a dynamically complex system that reacts quickly to subtle changes in control inputs or disturbances. If not controlled properly, the robot can become unstable within half a second. This complicates controller design, as a slight change in controller calibration or robot configuration can quickly destabilize the system.

[1]Taylor S. Clawson and Silvia Ferrari are with the Department of Mechanical and Aerospace Engineering, Cornell University, Ithaca, NY 14850 tsc83@cornell.edu, ferrari@cornell.edu

[2]Sawyer B. Fuller is with the Department of Mechanical Engineering, University of Washington, Seattle, WA

[3]Robert J. Wood is with the John A. Paulson School of Engineering and Applied Sciences and the Wyss Institute for Biologically Inspired Engineering, Harvard University, Cambridge, MA 02138

Fig. 1: A model of the RoboBee.

The sensitive dynamics present additional challenges, as the closed-loop system is highly sensitive to any time delay between sensing and control inputs. Biological flying insects are capable of completing 90° turns in less than $50ms$ [5]. The current RoboBee design flaps its wings at $120Hz$, corresponding to $8.3ms$ per wing-beat. A time delay of even $15ms$ in a robotic system would correspond to a delay of almost two full wing-beats, and would significantly complicate any attempts to maintain stability during rapid maneuvers.

To date, the RoboBee has been modeled using stroke-averaged forces [6], [7] for simulation and controller design. Additional models have been presented for the RoboBee using blade element theory to calculate instantaneous aerodynamic forces due to flapping wings, but have been limited to fixed platforms [8], [9]. In order to accurately predict aerodynamic force generation during flight, including how these forces vary as the robot rotates and translates through the air, this paper presents a model that combines blade element theory [10], [11] with rigid body dynamics to calculate the motion of the robot in flight. The approach in this paper is inspired by models that have been presented for modeling insect flight [12], [13]. A primary difference is that the RoboBee cannot actively control wing pitch, whereas most insects have control over all three wing degrees of freedom. In order to compare the model with flight test data, the controller presented in [1] is recreated and used to control the simulated model. The closed-loop dynamics are validated against real world flight test data to determine its

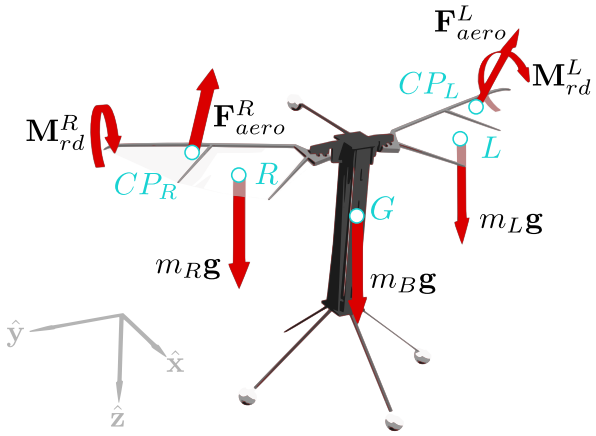

Fig. 2: Free body diagram for the RoboBee

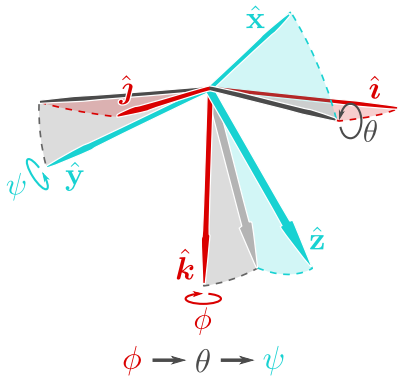

Fig. 3: The Euler Angle convention used to rotate from the fixed frame $\mathcal{F}$ ($\hat{\boldsymbol{\imath}}, \hat{\boldsymbol{\jmath}}, \hat{\boldsymbol{k}}$) to the body frame $\mathcal{B}$ ($\hat{\mathbf{x}}$, $\hat{\mathbf{y}}$, $\hat{\mathbf{z}}$).

effectiveness at predicting the motion of the robot in flight.

II. Model Description

As shown in Fig. 2, the RoboBee is modeled as three rigid, linked components: a left wing, right wing, and the body. Any warping that occurs in the wings during flight is ignored, as is any deformation of the components within the body. The wings are driven by piezoelectric actuators through independent transmission mechanisms as described in [14]. The signal is sent to the actuators through a tether connecting the robot to an external computer, which also provides power to the robot.

The design of the actuators plays an important role in the overall performance of the robot. The wings are designed to flap near their resonant frequency to maximize lift generation. Various components of the system, including the piezoelectric actuators and wing hinges, have recently been studied to increase the efficiency of the robot [9], [15]. In this paper, the actuators are assumed to be sufficiently powerful to drive the wings at the desired amplitude and frequency, and their dynamics are neglected. Various on board sensors have been developed recently for the application of untethered flight [6], [7]. Test flights are currently conducted in a lab environment with a Vicon system providing position sensing to the external computer.

Aerodynamic forces on the wings are computed using blade element theory as described in [10], [11], [16]. Blade element theory provides advantages over more complex models by providing a simple analytical model for the aerodynamic forces. Although blade element theory does not account for all aerodynamic forces acting on flapping wings, it has been shown to accurately model the dynamics of many different insect species in hovering flight [5], [16]. Previous RoboBee studies have shown relatively good agreement between blade-element wing models and test data [8].

A. Rigid Body Dynamics

The RoboBee body and both wings were assumed to be rigid. Although the wings flex slightly during flight, making this assumption greatly simplifies the calculation of both aerodynamic forces and resulting wing motions. The actuators oscillate within the body in the real robot, but since their movements oppose each other, changes to key parameters such as moment of inertia and center of gravity should be negligible. After constraining the wings to be attached at the top of the body, the state of each wing can be described entirely in terms of attitude and rotational velocity.

The entire system has 8 degrees of freedom in its configuration, comprised of 6 degrees of freedom for the body and 1 rotational degree of freedom for each wing. A free body diagram showing the forces and moments acting on the RoboBee is shown in Fig. 2. The coordinate frame shown in Fig. 2 is used throughout the following sections. The constraints on the degrees of freedom for the wings are described below. The rotation of each body is specified using the z-x-y Euler angle convention, with successive rotations measured by ϕ, θ, and ψ as shown in Fig. 3. This convention is used for both wings and the robot frame. The body frame $\mathcal{B}$ is defined with respect to the fixed frame $\mathcal{F}$ as shown in Fig. 3. Frames for the left wing $\mathcal{L}$ ($\hat{\mathbf{x}}_L$, $\hat{\mathbf{y}}_L$, $\hat{\mathbf{z}}_L$) and right wing $\mathcal{R}$ ($\hat{\mathbf{x}}_R$, $\hat{\mathbf{y}}_R$, $\hat{\mathbf{z}}_R$) are defined similarly, but with respect to the body frame $\mathcal{B}$.

The desired stroke angle ϕ of each wing is calculated by the control law and used as an input to the actuators. However, the actuators are not able to perfectly follow an arbitrary control signal. Since the system is being driven at resonance, any change in frequency will cause a corresponding drop in the peak-to-peak amplitude ϕ_0. Some test data on these effects can be found in [9], although no data is available for the step response to changes in mean amplitude ($\bar{\phi}$) and other flapping parameters. To account for these effects, the desired wing stroke signal $\phi(t)$ is filtered through a second-order transfer function tuned to represent the actuator dynamics. By fixing the resonant frequency of the transfer function to $120Hz$, the remaining parameters of the function can be adjusted to control additional key parameters including settling time and rise time.

The stroke plane deviation angle θ of each wing is held at 0, as in the physical robot. The pitch angle ψ of each wing is free to change according to the dynamics of the system, and is affected by aerodynamic forces, the restoring moment of the spring, and the acceleration of the body. The

motion of the system can be described by taking angular momentum balance of the entire system about the frame's center of gravity in (1), angular momentum balance of each wing about the hinge axis in (2), and linear momentum balance of the entire system in (3).

The angular momentum balance for the system is simplified by splitting up the contribution of each of the three components to both the total moment acting on the system and the change in angular momentum of the system. The total moment acting on the system is the sum of all moments contributed by the right wing $\sum \mathbf{M}_G^{\mathcal{R}}$ and left wing $\sum \mathbf{M}_G^{\mathcal{L}}$. The moment contributed by each wing is dominated by aerodynamic rotational damping ($\mathbf{M}_{rd}^{\mathcal{L}}$ and $\mathbf{M}_{rd}^{\mathcal{R}}$) and the moment caused by the total aerodynamic forces $\mathbf{F}_{aero}^{\mathcal{L}}$ and $\mathbf{F}_{aero}^{\mathcal{R}}$. No moments are contributed by the body, since the angular momentum balance is taken about the body's center of gravity. The angular momentum balance about the body center of gravity G is,

$$\sum \mathbf{M}_G^{\mathcal{L}} + \sum \mathbf{M}_G^{\mathcal{R}} = \dot{\mathbf{H}}_G^{\mathcal{B}} + \dot{\mathbf{H}}_G^{\mathcal{L}} + \dot{\mathbf{H}}_G^{\mathcal{R}} \tag{1}$$

where the individual moments can be expanded as:

$$\sum \mathbf{M}_G^{\mathcal{L}} = \mathbf{M}_{rd}^{\mathcal{L}} + \mathbf{r}_{CP_L/G} \times \mathbf{F}_{aero}^{\mathcal{L}} + \mathbf{r}_{L/G} \times m_L \mathbf{g}$$
$$\sum \mathbf{M}_G^{\mathcal{R}} = \mathbf{M}_{rd}^{\mathcal{R}} + \mathbf{r}_{CP_R/G} \times \mathbf{F}_{aero}^{\mathcal{R}} + \mathbf{r}_{R/G} \times m_R \mathbf{g}$$

The change in angular momentum for each of the three components is then expressed in terms of their inertia, angular rates, and the acceleration of the center of gravity for each component

$$\dot{\mathbf{H}}_G^{\mathcal{B}} = I_G^{\mathcal{B}} \dot{\boldsymbol{\omega}}_{\mathcal{B}} + \boldsymbol{\omega}_{\mathcal{B}} \times I_G^{\mathcal{B}} \boldsymbol{\omega}_{\mathcal{B}}$$
$$\dot{\mathbf{H}}_G^{\mathcal{L}} = I_G^{\mathcal{L}} \dot{\boldsymbol{\omega}}_{\mathcal{L}} + \boldsymbol{\omega}_{\mathcal{L}} \times I_G^{\mathcal{L}} \boldsymbol{\omega}_{\mathcal{L}} + \mathbf{r}_{L/G} \times m_L \mathbf{a}_L$$
$$\dot{\mathbf{H}}_G^{\mathcal{R}} = I_G^{\mathcal{R}} \dot{\boldsymbol{\omega}}_{\mathcal{R}} + \boldsymbol{\omega}_{\mathcal{R}} \times I_G^{\mathcal{R}} \boldsymbol{\omega}_{\mathcal{R}} + \mathbf{r}_{R/G} \times m_R \mathbf{a}_R$$

In the above equations, $\mathbf{r}_{CP_L/G}$ is the vector from the center of gravity of the frame G to the center of pressure of the left wing, $\mathbf{r}_{L/G}$ is the vector from the center of gravity of the body G to the center of gravity of the left wing L, m_L is the mass of the left wing, and $\mathbf{g}$ is the gravity vector. In all cases, $\mathcal{L}$ denotes left wing. The equivalent expressions for the right wing are denoted by $\mathcal{R}$.

The moments of inertia of the body, left, and right wings, respectively, are given by $I_G^{\mathcal{B}}$, $I_G^{\mathcal{L}}$, and $I_G^{\mathcal{R}}$. The angular rate of rotation is denoted as $\boldsymbol{\omega}$ and the angular acceleration is $\dot{\boldsymbol{\omega}}$, with subscripts $\mathcal{B}$, $\mathcal{L}$, and $\mathcal{R}$ denoting the frame. The mass of each wing is denoted by m_L and m_R, and the acceleration of the center of gravity in the fixed frame is denoted by $\mathbf{a}_L$ and $\mathbf{a}_R$ for each wing.

In addition to (1), the angular momentum balance of each wing is taken about A, the point where the wing attaches to the frame of the RoboBee, as shown in Fig. 4.

$$\sum \hat{\mathbf{y}}_W \cdot \mathbf{M}_A = \hat{\mathbf{y}}_W \cdot \dot{\mathbf{H}}_A \tag{2}$$

where

$$\sum \mathbf{M}_A = \mathbf{M}_{rd}^{\mathcal{W}} + (\mathbf{r}_{CP_W/A} \times \mathbf{F}_{aero}^{\mathcal{W}}) + (\mathbf{r}_{W/A} \times m_W \mathbf{g}) + \mathbf{M}_k$$
$$\dot{\mathbf{H}}_A = I_G^{\mathcal{W}} \dot{\boldsymbol{\omega}}_{\mathcal{W}} + \boldsymbol{\omega}_{\mathcal{W}} \times I_G^{\mathcal{W}} \boldsymbol{\omega} + \mathbf{r}_{W/A} \times m_W \mathbf{a}_W$$

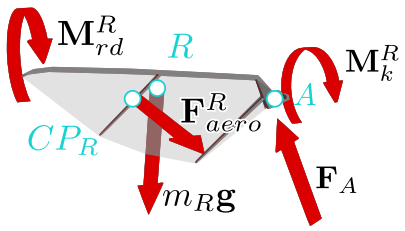

Fig. 4: Free body diagram for the right wing.

$\mathbf{F}_{aero}^{\mathcal{W}}$ denotes the total aerodynamic force on the wing and $\mathbf{M}_k$ is the rotational moment caused by the wing hinge. The W subscript or superscript on the variables is replaced with L or R for the left wing or right wing, respectively.

The linear momentum balance for the entire system is used to compute the translational acceleration of the body,

$$\sum \mathbf{F} = \sum m\mathbf{a} \tag{3}$$

where,

$$\sum \mathbf{F} = \mathbf{F}_{aero}^{\mathcal{R}} + \mathbf{F}_{aero}^{\mathcal{L}} + m_R\mathbf{g} + m_L\mathbf{g} + m_B\mathbf{g}$$
$$\sum m\mathbf{a} = m_B\mathbf{a}_G + m_R\mathbf{a}_R + m_L\mathbf{a}_L$$

m_B is the mass of the body and $\mathbf{a}_G$ is the acceleration of the body center of gravity G with respect to the fixed frame.

B. Aerodynamic Forces

The calculation of aerodynamic forces used in this model follows the approach presented in [8], where blade element theory is used to compute forces and moments on a wing mounted to a fixed plate, and the model is successfully validated with experimental data. In this paper, however, the motion of the wings is coupled with the motion of the robot body. Including body motion in the aerodynamic force calculations can have a significant impact on the forces generated during flight. Simulations of open-loop flight have shown that peak instantaneous aerodynamic forces are approximately 50% larger with body velocity $|\mathbf{v}_{\mathcal{B}}| \approx 1m/s$ and angular velocity $|\boldsymbol{\omega}_{\mathcal{B}}| \approx 30rad/s$, both of which are in the range of values typically observed during flight. The dependence of aerodynamic force generation on angular velocity, $\boldsymbol{\omega}_{\mathcal{B}}$, in particular makes stabilizing the robot challenging, as angular velocities can increase rapidly during flight, dramatically changing instantaneous forces on the robot.

The general form for all aerodynamic forces and moments computed here is,

$$dF_{aero} = C_F(\alpha) dS q \tag{4}$$

where dF is the magnitude of the force or moment on a differential wing element, $C_F(\alpha)$ is the force coefficient, α is the angle of attack, $q = \frac{1}{2}\rho \mathbf{V}_{\delta w} \cdot \mathbf{V}_{\delta w}$ is the dynamic pressure at the wing element, and dS is a reference area. The dynamic pressure is a function of the local velocity of the wing element i.e., $\mathbf{V}_{\delta w} = \mathbf{V}_G + \mathbf{V}_{A/G} + \mathbf{V}_{\delta w/A}$. Also, ρ is the density of the ambient air, $\mathbf{V}_G$ is the velocity of the center of mass of the robot body G, $\mathbf{V}_{A/G}$ is the velocity

of the point A (as shown in Fig. 4) with respect to G, and $\mathbf{V}_{\delta w/A}$ is the velocity at the leading edge of the differential element with respect to point A (Fig. 4).

Using blade-element theory, each wing is decomposed into a number of chord-wise elements. An aerodynamic force is then computed for each element as a function of the local angle of attack and wing velocity relative to the free stream. These aerodynamic forces can be integrated along the length of the wing, yielding a total aerodynamic force for each wing ($\mathbf{F}^{\mathcal{R}}_{aero}$ and $\mathbf{F}^{\mathcal{L}}_{aero}$) acting at an instantaneous center of pressure (CP_R and CP_L). These forces are translational aerodynamic forces, and can be broken up into lift and drag components that are orthogonal to and parallel with the free stream velocity, respectively. Integrating (4) along the wing span yields,

$$F_{aero} = C_F(\alpha)\frac{1}{2}\rho\bar{c}R\int_0^1 \mathbf{V}_{\delta w}\cdot\mathbf{V}_{\delta w}\hat{c}(\hat{r})d\hat{r} \qquad (5)$$

where $\bar{c}$ is the mean chord length, R is the wing length, $\hat{c}(\hat{r}) = c(r)/\bar{c}(r)$ is the non-dimensionalized chord length, and $\hat{r} = r/R$ is the non-dimensionalized span-wise coordinate. The expressions for lift and drag coefficients presented in [17] are adopted here.

The span-wise location of the center of pressure (y_{CP}) is a function of the wing shape and remains mostly constant during flight [18] . The chord-wise location however (z_{CP}), is a function of the angle of attack (α) and thus varies during flight. The non-dimensionalized distance from the leading edge of the wing ($\hat{d}_{CP}$) is a convenient metric for computing the location of the center of pressure. Experimental data for *Drosophila*, obtained in [18] is used to determine the location for this model as well:

$$\hat{d}_{CP} = \frac{0.82}{\pi}|\alpha| + 0.05 \qquad (6)$$

In addition to the translational aerodynamic forces, a rotational damping term for each wing ($\mathbf{M}^{\mathcal{R}}_{rd}$ and $\mathbf{M}^{\mathcal{L}}_{rd}$) is included in the model. Experiments on passively rotating wings showed that neglecting this term results in predictions that are severely under-damped. This damping term creates a moment about the hinge axis of each wing.

The rotational damping moment is computed by using a modified version of (4), considering a moment as the generalized force and using a dynamic pressure q based on the rotational velocity of the wing about the hinge axis. This approach yields the damping moment for a differential element of height dz and width dy:

$$dM_{rd} = -C_{rd}\frac{1}{2}\rho(\omega_y z)^2|z|dydz \qquad (7)$$

where ω_y is the rotational velocity about the hinge axis and z is the distance from the hinge axis to the differential element. Integrating in the z and y directions yields the final expression for the rotational damping moment,

$$M_{rd} = -\frac{1}{2}C_{rd}\rho\omega_y^2\int_0^R\int_{z_0}^{z_{le}}|z^3|dzdy \qquad (8)$$

where z_{le} is the z-coordinate of the leading edge of the wing and z_0 is the z-coordinate of the trailing edge.

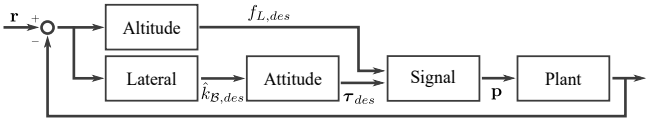

Fig. 5: Simplified block diagram of the system.

III. Controller

Accurately modeling the controller used in flight testing is an important part of the complete RoboBee model. In the absence of feedback control, the robot is unstable and tumbles rapidly just after takeoff. Any amount of flight data substantial enough to be used to validate a simulation must therefore come from controlled flights. To facilitate the comparison with flight data, the controller used to validate the model must match the controller used during flight tests as closely as possible. The flight test controller is described in [1], and consists of several distinct components, shown in Fig. 5. The altitude and lateral controllers generate a desired lift force and torque ($f_{L,des}$ and $\boldsymbol{\tau}_{des}$), which are then converted into flapping parameters $\mathbf{p}$ by the *Signal* block. The flapping parameters are used to generate input signals to control the trajectory of each wing.

The desired thrust $f_{L,des}$ is calculated by the altitude controller. The altitude controller consists of a PID controller with an additional feedforward component to offset the weight of the RoboBee. The controller used in testing also includes several low pass filters and additional switching components to enable smooth transitions between control inputs.

The desired torque is computed from a series of two controllers: a lateral controller followed by an attitude controller. The lateral controller is a PID controller that computes a desired body orientation $\hat{\mathbf{z}}_{des}$ based on the error in the $\hat{\boldsymbol{\imath}}$ and $\hat{\boldsymbol{\jmath}}$ directions. The attitude controller is another PID controller that computes desired torque values based on the error between the desired body orientation and the current body orientation. Similarly to the altitude controller, both the lateral and attitude control blocks contain several components designed to smooth the transitions between abrupt changes in commanded control inputs.

The flapping parameters generated by the *Signal* block in Fig. 5 adjust the motion of the wings to accomplish different maneuvers as shown in Fig. 6. A pitch offset ϕ_p adjusts the mean stroke angle $\bar{\phi}$ of both wings, a roll offset ϕ_r adjusts the relative stroke amplitude ϕ_0 of one wing relative to the other. The controller used for the flight tests shown in this paper did not actively control yaw, instead relying on the passive yaw damping of the robot.

The control structure used in the model is designed to closely mimic the structure and parameters used in the flight tests. The parameters used in the control blocks shown in Fig. 5 are identical to the parameters used in the flight tests. For simplicity, the controller used in the model omitted many of the low pass filters and other smoothing blocks used in flight tests. Many of the parameters used in those components

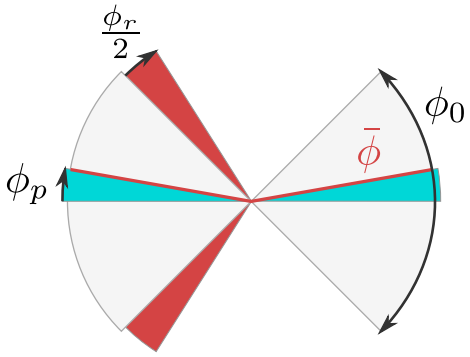

Fig. 6: Effects of various flapping parameters on wing trajectories

were not recorded in the flight data and the design of these components could therefore not be guaranteed to be identical between the flight data and the model. The desired effect of these blocks to mitigate abrupt changes to control inputs can be incorporated into the second-order transfer function used to model the actuator dynamics.

IV. Model Validation

Validating the model against experimental flight data is complicated by a number of factors. The dynamics of the RoboBee are sensitive to small variations in parameters that occur during manufacturing. It is not practical to obtain precise measurements for the exact values of all important parameters (such as mass, inertia, wing and body lengths, and actuator response) for every flight. The sensitivity of the response to slight variations in these parameters makes it impossible to exactly recreate a previously observed flight.

An additional complication is the natural instability of the RoboBee in flight. Any reasonable amount of flight data can be obtained only during a controlled flight of the robot. Validating a simulated flight against flight data obtained from experiments thus involves, in addition to the physical parameters of the robot, the parameters used in the controller for the flight test.

These complications have lead to an attempt to qualitatively validate the flight path taken by the simulated RoboBee. Additionally, an uncontrolled flight is simulated, in which instability was observed that matches the description in [7].

A. Forced Response

An important first step in validating the model involves examining the forced pitching response observed during any flight. A key observation is that the body pitches as the wings flap, as shown in Fig. 7. As the wings flap, the body pitch angle ψ oscillates at the same frequency. The mean peak-to-peak amplitude of this periodic response in flight tests was approximately $2.2°$. In the simulation, the same amplitude averaged approximately $2.5°$, which is 14% different than the experimentally recorded values. The drift observable in the experimental data in Fig. 7 is due to imperfect hovering,

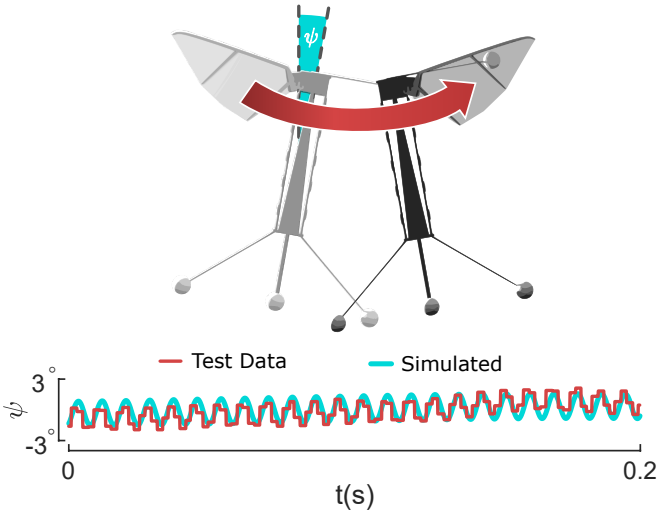

Fig. 7: Wing flapping causes oscillations in body pitch angle.

in which the stroke-averaged body pitch varied throughout the hovering test.

The additional pitching motion predicted by the model could correspond to an overestimate of instantaneous aerodynamic forces on the wings. Some of the discrepancy can be accounted for by the low sampling rate relative to the frequency of oscillation. This can be observed in Fig. 7 by comparing the test data and the simulated data from the model. The test data is frequently sampled away from the peak amplitudes, causing the lower average peak-to-peak value. The data shown in Fig. 7 is a small sample from similar regions in the test data and the simulated data after the robot has approached steady hovering flight. The data shown is representative of the good agreement between the model and the test data in comparable regions of flight.

B. Uncontrolled Flight

Previous studies have noted that the RoboBee is unstable in uncontrolled flight, in part due to aerodynamic drag on the wings. As the robot tips forwards, the net lift force tips in approximately the same direction, accelerating the body laterally. This increases drag on the wings, which tips the body in the reverse direction. In the current robot configuration, the aerodynamic drag tips the robot in the reverse direction before stopping its forward motion, resulting in growing oscillations that result in tumbling [7], [19].

This behavior was observed in the simulated flight paths generated by the model when using an open-loop flight controller. Figure 8 shows a time lapse of the trajectory of an uncontrolled flight for both an actual flight test (top) and the simulation (bottom). The oscillations described earlier can be clearly observed as the robot pitches forward and accelerates before the drag on the wings flips the body in the other direction. Although the simulation exhibits similar behavior to the flight test, the robot transitioned to tumbling motion more quickly than the simulation predicted, as can be seen by the red body-axis lines (spaced at even intervals of time) shown in each image.

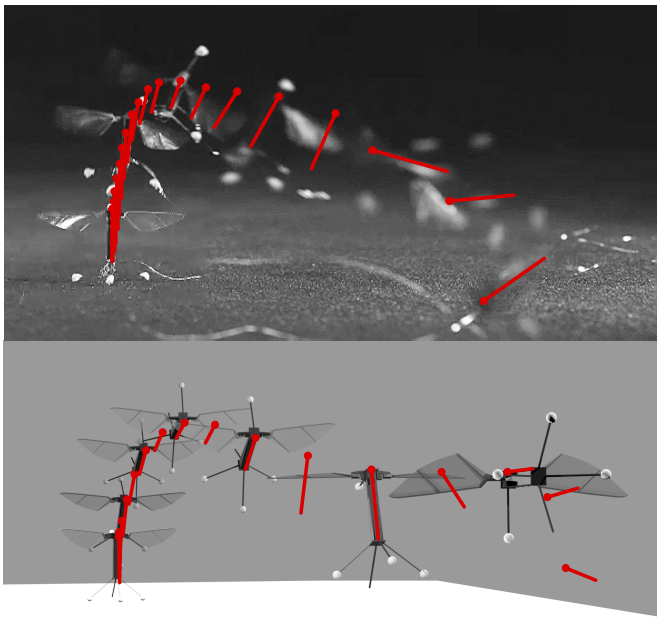

Fig. 8: Comparison of tested (top) and simulated (bottom) uncontrolled flight.

C. Controlled Flight

The simulations of actively controlled flight were performed using a controller design that closely mirrored the controller used during the flight tests as described in Section III. In the robot, the commanded torques and subsequent flapping parameter commands are attenuated, because the actuator dynamics act as a low-pass filter. The actuator dynamics were modeled as a linear second-order transfer function, the parameters of which were set to mimic the physical system, with a resonant peak at $120Hz$ and the damping ratio ζ used as a tuning parameter. Ultimately, choosing an underdamped system with $\zeta \approx 0.14$ showed good agreement with experimental data.

Figure 9 shows the trajectory from a RoboBee test flight. Using the same starting point and target waypoint, Fig. 10 shows the trajectory from a simulated flight using the model. A static pitch bias $\phi_p = 2°$ and roll bias $\phi_r = 2°$ were chosen for the simulation. Biases such as these are commonly observed in the physical robots due to manufacturing imperfections. The simulated model shows a smaller steady state error compared to the test flight, and approaches the waypoint more directly.

V. Conclusion

The approach presented here is generally applicable to *insect*-scale flapping robots, and captures much of the important behaviors observed in experimental RoboBee flights. It incorporates an accurate aerodynamic model with rigid-body dynamics to provide a good starting point for assessing potential controllers and possible physical design changes. It has been shown to agree reasonably well with the general flight characteristics of the robot, and is capable of modeling

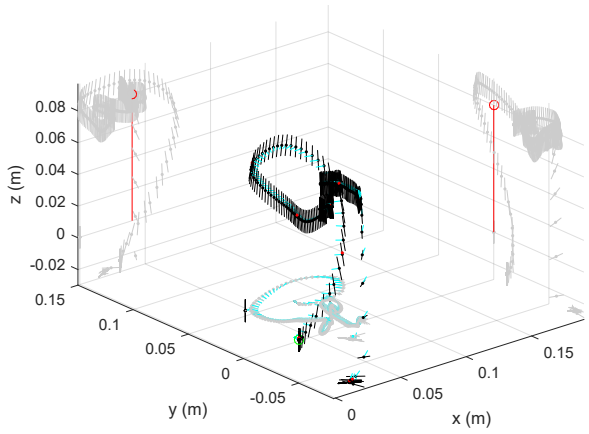

Fig. 9: RoboBee flight test data.

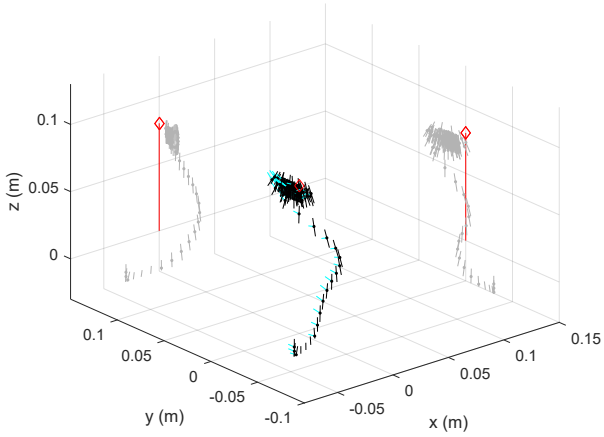

Fig. 10: Simulated flight with a 2° roll and pitch bias.

imperfections in manufactured units which existing models do not account for.

Acknowledgment

This research was funded by the National Science Foundation grants ECCS-1545574 and the Wyss Institute for Biologically Inspired Engineering.

References

[1] K. Y. Ma, P. Chirarattananon, S. B. Fuller, and R. J. Wood, "Controlled flight of a biologically inspired, insect-scale robot," *Science*, vol. 340, no. 6132, pp. 603–607, 2013. [Online]. Available: http://science.sciencemag.org/content/340/6132/603

[2] A. T. Baisch, O. Ozcan, B. Goldberg, D. Ithier, and R. J. Wood, "High speed locomotion for a quadrupedal microrobot," *The International Journal of Robotics Research*, p. 0278364914521473, 2014.

[3] M. Graule, P. Chirarattananon, S. Fuller, N. Jafferis, K. Ma, M. Spenko, R. Kornbluh, and R. Wood, "Perching and takeoff of a robotic insect on overhangs using switchable electrostatic adhesion," *Science*, vol. 352, no. 6288, pp. 978–982, 2016.

[4] Y. Chen, E. F. Helbling, N. Gravish, K. Ma, and R. J. Wood, "Hybrid aerial and aquatic locomotion in an at-scale robotic insect," in *Intelligent Robots and Systems (IROS), 2015 IEEE/RSJ International Conference on*. IEEE, 2015, pp. 331–338.

[5] S. N. Fry, R. Sayaman, and M. H. Dickinson, "The aerodynamics of free-flight maneuvers in drosophila," *Science*, vol. 300, no. 5618, pp. 495–498, 2003.

[6] S. B. Fuller, E. F. Helbling, P. Chirarattananon, and R. J. Wood, "Using a mems gyroscope to stabilize the attitude of a fly-sized hovering robot," in *IMAV 2014: International Micro Air Vehicle Conference and Competition 2014, Delft, The Netherlands, August 12-15, 2014*. Delft University of Technology, 2014.

[7] S. B. Fuller, M. Karpelson, A. Censi, K. Y. Ma, and R. J. Wood, "Controlling free flight of a robotic fly using an onboard vision sensor inspired by insect ocelli," *Journal of the Royal Society Interface*, vol. 11, 2014.

[8] J. Whitney and R. Wood, "Aeromechanics of passive rotation in flapping flight," *Journal of Fluid Mechanics*, vol. 660, pp. 197–220, 2010.

[9] N. T. Jafferis, M. A. Graule, and R. J. Wood, "Non-linear resonance modeling and system design improvements for underactuated flapping-wing vehicles," in *2016 IEEE International Conference on Robotics and Automation (ICRA)*. IEEE, 2016, pp. 3234–3241.

[10] C. Ellington, "The aerodynamics of hovering insect flight. i. the quasi-steady analysis," *Philosophical Transactions of the Royal Society of London B: Biological Sciences*, vol. 305, no. 1122, pp. 1–15, 1984.

[11] Z. J. Wang, "Dissecting insect flight," *Annu. Rev. Fluid Mech.*, vol. 37, pp. 183–210, 2005.

[12] S. Chang and Z. J. Wang, "Predicting fruit flys sensing rate with insect flight simulations," *Proceedings of the National Academy of Sciences*, vol. 111, no. 31, pp. 11 246–11 251, 2014.

[13] W. B. Dickson, A. D. Straw, and M. H. Dickinson, "Integrative model of drosophila flight," *AIAA journal*, vol. 46, no. 9, pp. 2150–2164, 2008.

[14] K. Y. Ma, S. M. Felton, and R. J. Wood, "Design, fabrication, and modeling of the split actuator microrobotic bee," in *2012 IEEE/RSJ International Conference on Intelligent Robots and Systems*. IEEE, 2012, pp. 1133–1140.

[15] N. T. Jafferis, M. J. Smith, and R. J. Wood, "Design and manufacturing rules for maximizing the performance of polycrystalline piezoelectric bending actuators," *Smart Materials and Structures*, vol. 24, no. 6, p. 065023, 2015.

[16] S. P. Sane and M. H. Dickinson, "The control of flight force by a flapping wing: lift and drag production," *Journal of experimental biology*, vol. 204, no. 15, pp. 2607–2626, 2001.

[17] Z. J. Wang, J. M. Birch, and M. H. Dickinson, "Unsteady forces and flows in low reynolds number hovering flight: two-dimensional computations vs robotic wing experiments," *Journal of Experimental Biology*, vol. 207, no. 3, pp. 449–460, 2004.

[18] W. B. Dickson, A. D. Straw, C. Poelma, and M. H. Dickinson, "An integrative model of insect flight control," in *Proceedings of the 44th AIAA Aerospace Sciences Meeting and Exhibit*, 2006, pp. 31–38.

[19] L. Ristroph, G. Ristroph, S. Morozova, A. J. Bergou, S. Chang, J. Guckenheimer, Z. J. Wang, and I. Cohen, "Active and passive stabilization of body pitch in insect flight," *Journal of The Royal Society Interface*, vol. 10, no. 85, p. 20130237, 2013.